Accelerated deactivation studies of the natural-gas oxidation catalyst—Verifying the role of sulfur and elevated temperature in catalyst aging

Mari Honkanen [a,*], Marja Kärkkäinen [b], Tanja Kolli [b], Olli Heikkinen [c], Ville Viitanen [c], Lunjie Zeng [d], Hua Jiang [c], Kauko Kallinen [e], Mika Huuhtanen [b], Riitta L. Keiski [b], Jouko Lahtinen [c], Eva Olsson [d], Minnamari Vippola [a]

[a] Department of Materials Science, Tampere University of Technology, P.O. Box 589, 33101 Tampere, Finland
[b] Environmental and Chemical Engineering, Faculty of Technology, University of Oulu, P.O. Box 4300, 90014 Oulu, Finland
[c] Department of Applied Physics, Aalto University, P.O. Box 14100, 00076 Aalto, Finland
[d] Department of Applied Physics, Chalmers University of Technology, 41296 Gothenburg, Sweden
[e] Dinex Ecocat Oy, Typpitie 1, 90620 Oulu, Finland

A R T I C L E   I N F O

A B S T R A C T

Accelerated deactivation, caused by thermal aging (TA) and/or sulfur + water poisoning (SW), of the PtPd/γ-Al$_2$O$_3$ natural-gas oxidation catalyst was studied. Thermal aging and poisoning treatments were performed separately and with varied combinations and comprehensive characterization of the catalyst was carried out after each step. The fresh catalyst has small, oxidized PtPd particles (<5 nm) uniformly distributed in the γ-alumina washcoat. After the SW-treatment, a small amount of bulk aluminum sulfate was observed near the slightly grown noble metal particles. During the thermal aging, γ-alumina changed to δ-/θ- and α-alumina. In addition, total decomposition of oxidized Pt and partly decomposition of oxidized Pd occurred resulting in the formation of the grown noble metal particles with a bimetallic PtPd core and a polycrystalline PdO shell. Also few, small (~5 nm) bimetallic PtPd particles were still detected. In the TA + SW-treated catalyst with grown noble metal particles, a small amount of bulk aluminum sulfate was detected and it was randomly distributed over the noble metal particles and washcoat. The activity in the terms of methane conversion over the TA-, SW-, and SW + TA-treated catalysts was similar but it was decreased compared to the fresh catalyst. The activity of the TA + SW-treated catalyst was drastically decreased compared to the fresh catalyst due to significant morphological changes and aluminum sulfate formation.

1. Introduction

Natural gas (NG) is a potential sustainable energy source for vehicles and engines as its environmental impacts are smaller than those of e.g., crude oil-based fuels. For example exhaust emissions of the natural gas vehicles (NGVs) are much lower than those in the diesel vehicles. However, exhaust gases of NGVs contain unburned methane and carbon monoxide, a potential greenhouse gases, and thus catalytic oxidation converters are needed [1,2]. Supported palladium catalysts are widely known to be active for methane combustion and it is agreed that PdO is the active phase while metallic palladium is much less active. Pd $\leftrightarrow$ PdO transformation is reversible and according to Farrauto et al. [3], decomposition temperature of PdO to Pd in the PdO/Al$_2$O$_3$ catalyst is ~800 °C and reformation temperature of Pd to PdO during cooling is ~600 °C. Hysteresis in the reformation is due to strongly bound oxygen on the Pd surface inhibiting bulk oxidation [4]. Many other factors, such as gas phase composition and pressure, type of support, additives and contaminants, and pretreatment conditions, have also effects on the Pd $\leftrightarrow$ PdO transformation [5]. In addition, several studies have reported that the activity and stability of Pd catalysts in methane combustion can be improved by adding Pt into the catalyst to decelerate sintering of Pd and PdO, e.g., [6–9].

Deactivation of the catalyst, caused by poisoning and thermal aging, is a problem also in the natural gas applications. Poisoning is

due to adsorption of impurities, e.g., S, P, Zn, Ca, and Mg, present in the exhaust gases, on the catalytic active sites. Poisons can also react with the active sites followed by formation of non-active compounds [10]. Sulfur is known to be one of the most important components for deactivation of the Pd catalysts for methane oxidation [11] and only a small amount of SO_2 significantly decreases catalyst activity by blocking the active noble metal sites by sulfur compounds [12]. It is known that sulfur in the NGV exhaust gas originates from odorants and lubricating oils and from gas itself. Under the typical natural-gas engine conditions, with large excess of air and with an oxidation catalyst, sulfur will be oxidized to SO_2 and SO_3. Above 300 °C, a catalyst has enough activity for the oxidation of SO_2 to SO_3 [10]. Metallic Pt on the PtPd catalysts is found to be active to adsorb sulfur compounds. Therefore, the presence of metallic Pt prevents adsorption of sulfur on the Pd surface sites which are then available for methane oxidation [13]. Also the catalyst washcoat affects sulfur poisoning. For example Pd/Al_2O_3 catalysts deactivate less than Pd/SiO_2 catalysts due to adsorption of SO_x also on the Al_2O_3 washcoat material [11]. According to Mowery and McCormick [14], when SO_2 and water exist, the sulfation of the PdO/Al_2O_3 catalyst happens by oxidation of SO_2 to SO_3 on PdO and further SO_3 over PdO can form $PdSO_4$ or can migrate to Al_2O_3 forming $Al_2(SO_4)_3$. The sulfation is reversible and SO_x from the catalyst surface easily desorbs already below 400 °C and more stable washcoat sulfates decompose above 700 °C [15]. SO_2 can affect also the acidity of the Al_2O_3 support. Konsolakis et al. [16] noticed that the fresh Pd/γ-Al_2O_3 catalyst has only Lewis acid sites but SO_2 treatment increases significantly Brönsted acid sites on the γ-Al_2O_3 support. According to Wischert et al. [17], the reactivity of γ-Al_2O_3 towards methane is due to the highly reactive Lewis acid-base pairs (Al,O) enabling low-energy pathways for the dissociation of C—H bond in methane.

Thermal deactivation of a catalyst is reported to be caused by: (a) loss of active surface area due to crystallite growth of the noble metal particles and due to pore collapse on crystallites of the active phase, (b) loss of support area due to collapse of the washcoat and/or (c) chemical transformations of active catalytic phases to non-active phases. In general, sintering occurs at elevated temperatures (>500 °C) and is accelerated by water vapor [18]; the driving force for sintering is to minimize surface energy and it is reduced with the transport, growth, and coalescence of the particles [10].

Two mechanisms for sintering of catalyst nanoparticles have been proposed: particle migration followed by coalescence (PMC) and Ostwald ripening (OR). In the particle migration, sintering occurs by migration of the whole crystallites along the support surface and coalescence of the crystallites forms larger particles. OR is migration of single metal atoms or molecular species from small particles to large ones; larger particles grow at the expense of smaller particles [10,18–21]. Hansen et al. [19] studied the mechanism of the catalyst nanoparticle sintering mainly by in situ transmission electron microscopy. They noticed that the early stage of the sintering is dominated by OR and surface area increases rapidly caused by the disappearance of the smallest particles. In the further stage, grown particles coalesce when they are close to each other. Sintering becomes slower when particles grow and the distance between them increases [19]. Many factors e.g., temperature, atmosphere, metal type, support, and impurities affect the rate of noble metal sintering. The sintering rate increases exponentially with elevated temperature and metals sinter faster in oxygen than in hydrogen atmosphere [18]. Generally, sintering of the noble metal clusters is accelerated by the presence of gases; Parkinson et al. [22] reported that existence of carbon monoxide induced coalescence of Pd atoms in the Pd/Fe_3O_4 system and that formed Pd-carbonyl species were responsible for increased Pd mobility. Water vapor has also been found to accelerate sintering. In reducing atmosphere, the stability of the metal crystallites typi-

cally decreases with decreasing noble metal melting temperature. In oxidizing atmosphere, stability depends on the volatility of metal oxides and on the noble metal–support interactions [18]. In addition, the position of the noble metal particles affects the rate of sintering; a valley position is much more stable than an on-top position [21]. Pores in the support hinder the mobility of the metal crystallites; especially if pore diameters are about same size as the crystallites [18]. Impurities affect the sintering rate, for example sulfur increases mobility of the metal atoms [18,23,24] while for example calcium is found to decrease it [18].

In the case of the catalysts with an alumina washcoat, phase transformations of the support may occur; γ-alumina with high specific surface area can change to δ-alumina and finally via θ-alumina to stable α-alumina [10]. Phase transformation results in sintering or grain growth followed by a decrease in the surface area [25]. According to Wischert et al. [17], the phase transformation of γ-Al_2O_3 to θ-Al_2O_3 causes the reconstruction of the surface resulting in decrease of highly reactive sites for methane.

In the real vehicle aging conditions, deactivation process is a complex phenomenon and e.g., both thermal aging and poisoning exist. In our earlier study [26], the natural-gas heavy-duty-vehicle-aged (160,000 km) $PtPd/\gamma$-Al_2O_3-based catalyst was studied. Significant morphological changes and chemical poisoning were detected compared to the fresh catalyst and this has led to drastic deactivation in methane conversion. It was difficult to conclude which changes were caused by thermal aging and which by chemical poisoning. Thus, detailed studying of deactivation phenomena in the vehicle-aged catalysts was found very challenging. Sulfur poisoning of the oxidation catalysts is widely studied, e.g., [10,11,13–15,18]. In this study, sulfur poisoning and thermal aging were studied separately and with varied combinations enabling detailed analysis of the role of sulfur in the catalyst and effects of thermal aging before or after sulfur poisoning. This kind of in-depth knowledge gained is crucial in the development of efficient exhaust emission reduction systems for NGVs.

2. Experimental

2.1. Catalyst material

The studied material was a PtPd (1:4 wt-%) catalyst supported on γ-alumina washcoat on the metallic monolith. The studied catalyst was manufactured and designed by Dinex Ecocat Oy for lean-burn natural gas applications. Total metal loading in the catalyst was 8.8 g/dm^3 and the catalyst was calcined at 550 °C for 4 h. The catalyst was studied as fresh and after various chemical and thermal laboratory-scale accelerated deactivation treatments.

2.2. Laboratory-scale accelerated deactivation treatments

Laboratory-scale sulfur + water treatment (SW) and thermal aging (TA) treatment were carried out to find out detailed knowledge about deactivation phenomena of the $PtPd/\gamma$-Al_2O_3 oxidation catalyst for natural-gas applications. SW-treatment was performed in the following conditions: 100 ppm SO_2, 10 vol-% H_2O, 10 vol-% air, balanced with N_2. The quartz tube reactor was heated from room temperature to 400 °C in a nitrogen and air flow with the heating rate of 10 °C/min. After 5 h of the SW-treatment, the reactor was cooled down to the room temperature in nitrogen and air flow. The gas hourly space velocity (GHSV) was 20,000 h^{-1} during the treatment. Thermal aging was carried out in the tube reactor under synthetic air (80% N_2 + 20% O_2) at 1000 °C for 5 h. The used temperature was above the normal operation temperature of the catalysts but it was chosen to mimic an accelerated thermal aging and thus the long-term behavior of the catalyst. Temperature for

Table 1
Laboratory-scale treatments and corresponding markings.

Marking	Treatment
Fresh	As-received from Dinex Ecocat Oy
SW	Sulfur + water poisoning (100 ppm SO_2 + 10 vol-% H_2O + 10 vol-% air + N_2 (bal.), 400 °C/5 h)
TA	Thermal aging at 1000 °C/5 h (80 vol-% N_2 + 20 vol-% O_2)
TA + SW	Thermal aging followed by sulfur + water poisoning
SW + TA	Sulfur + water poisoning followed by thermal aging

the TA-treatment was chosen based on our tentative study about laboratory-scale thermal aging treatments for natural gas oxidation catalyst (various temperatures between 400 °C and 1100 °C); with this thermal aging temperature, the catalyst structure changes similar to a vehicle-aged catalyst were achieved [26]. The catalyst samples were set into the tubular ceramic furnace when the treatment temperature was reached, then the gas flow was switched on. After the treatment period the gas flow was switched off and the catalyst samples were removed from the furnace and let to cool down to room temperature. TA- and SW-treatments were performed separately and with varied combinations (Table 1). Detailed characterization of the catalyst was carried out after each step.

2.3. Characterizations

The structure of the fresh and treated catalysts was studied by scanning electron microscopy (SEM), transmission electron microscopy (TEM), and X-ray diffractometry (XRD). A field-emission SEM (FESEM, Zeiss ULTRAplus) is equipped with an energy dispersive spectrometer (EDS, INCAx-act silicon-drift detector (SDD), Oxford Instruments). Cross-sectional FESEM samples were prepared with a conventional metallographic sample preparation technique by molding the catalyst samples into resin followed by grinding and polishing and carbon coating to avoid sample charging during the FESEM studies. All the presented cross-sectional FESEM images were taken with an angular selective backscatter (AsB) detector to maximize Z-contrast. Three different TEMs were used to characterize the samples. A TEM (Jeol JEM-2010) equipped with an EDS (Noran Vantage Si(Li) detector, Thermo Scientific) was used for imaging and elemental analysis. A high resolution TEM (HRTEM, Jeol 2200FS) with two aberration correctors (CEOS GmbH) equipped with EDS (Jeol Si(Li) detector) was used for high resolution imaging and elemental analysis. A high resolution TEM/scanning TEM (STEM, FEI Titan 80-300) with a probe C_S corrector, a Gatan Imaging Filter (GIF, Tridium), and an EDS (INCAx-sight Si(Li) detector) was used for high resolution imaging, electron energy loss spectroscopy (EELS), and elemental analysis. Annular dark field (ADF) STEM images were acquired using a 17.5 mrad beam convergence angle and ∼54–270 mrad detector collection angle. The collection angle for EELS is ∼24 mrad. Cross-sectional TEM samples from the fresh catalyst and from the TA + SW-treated catalyst were prepared as follows. Small pieces of the catalyst monolith were attached the washcoats face-to-face to a titanium grid by carbon glue. The grid was pre-thinned by hand to the thickness of ∼70 μm and then with a dimple grinder (Model 565, Gatan Inc.) to the thickness of ∼20 μm. The final thinning for electron transparency was made with a precision ion polishing system (PIPS, Model 691, Gatan Inc.). Powdered TEM samples from all studied catalysts were prepared by crushing the scraped catalyst powder between two laboratory glass slides and dispersing the crushed powder with ethanol onto a copper grid with a holey carbon film. Scraped catalyst powders were used also for XRD studies (Empyrean with the PIXcel³D detector, PANalytical, using Cu Kα radiation). Crystallite sizes were determined from the XRD patterns with the aid of the HighScore plus software based on the Scherrer equation (shape factor 0.9) and phases were identified by using the

database (PDF-4 + 2014) from International Centre for Diffraction Data (ICDD).

The chemical state and composition of the fresh and treated catalysts were studied by X-ray photoelectron spectroscopy (XPS, SSX-100, Surface Science Instruments, using monochromatic Al Kα radiation). For XPS measurements, a small amount of the scraped catalyst powder was pressed into a piece of indium and the samples were pre-treated in high vacuum for a few hours before measurements. The binding energy values in the acquired spectra were calibrated by setting carbon 1s line at 284.6 eV. Carbon and indium were excluded from the compositional analysis. In quantitative analysis, Shirley background subtraction was applied [27].

Specific surface areas, pore sizes, and pore volumes of the fresh and treated catalysts were determined using the Micrometrics ASAP 2020 device. Specific surface areas were measured from the N_2 adsorption isotherms at −196 °C according to the standard BET (Brunauer–Emmett–Teller) method. Pore size and pore volume distributions of catalysts were calculated from N_2 desorption isotherms by the BJH (Barrett–Joyner–Halenda) method.

A Fourier transform infrared (FT-IR) spectrometer (Bruker Vertex V80) equipped with a diffuse reflectance infrared Fourier transform (DRIFT) unit and a liquid nitrogen-cooled mercury cadmium telluride (MCT) detector was utilized to find the information about the bonding of the compounds on the scraped catalyst powder. The DRIFT analyses were performed at room temperature under normal atmosphere conditions. The mirror was used as a background spectrum. Spectra were recorded by using a resolution of 4 cm^{-1}.

Laboratory scale light-off tests were used to define catalyst activity before and after SW-, TA-, TA+SW-, and SW+TA-treatments. Catalytic activities were determined in lean reaction conditions using the following gas mixture: 600 ppm CH_4, 500 ppm CO, 10 vol-% CO_2, 12 vol-% O_2, 10 vol-% H_2O, and N_2 as balance gas. The total gas flow was 1 dm³/min resulting in a GHSV of 31,000 h^{-1}. The measurements were carried out at atmospheric pressure in a horizontally aligned tubular quartz reactor. The temperature of the catalyst bed was increased from room temperature up to 600 °C with a linear heating rate of 10 °C/min. H_2O was added at 110 °C with a peristaltic pump. The catalyst was kept at steady state for 15 min at 600 °C and after that the furnace was cooled down to room temperature under the N_2 flow. The procedure was repeated (run 1 and run 2). If not specifically mentioned, the data of the catalyst activities was taken from the second run. Gas flow rates were controlled by using mass flow controllers (Brooks 5280S). The outlet gas composition was analyzed as a function of temperature by a Gasmet™ FT-IR gas analyzer. Oxygen concentration was determined by using a paramagnetic oxygen analyzer (ABB Advanced Optima).

3. Results and discussion

3.1. Structural characteristics of the catalyst

Structural characteristics of the fresh and treated catalysts were studied by several methods. Based on the FESEM studies, the structure of the fresh and SW-treated catalyst was similar. Moreover,
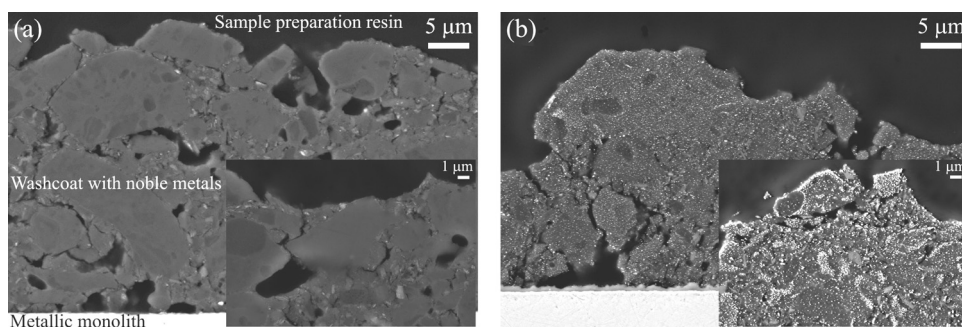
Fig. 1. Cross-sectional FESEM (AsB) images, higher magnifications as insets, (a) the fresh catalyst and (b) the TA+SW-treated catalyst, white spots represent the grown noble metal particles.

the structures of the TA-, TA + SW-, and SW + TA-treated catalysts were observed to be analogous. Cross-sectional AsB images of the fresh and TA+SW-treated catalyst are presented in Fig. 1(a) and (b), respectively. In the fresh and SW-treated catalysts, the noble metal particles were too small to be detected with FESEM. In the TA-, TA + SW-, and SW + TA-treated catalysts, the particle size of the noble metals was increased significantly through the catalysts (white spots in Fig. 1(b)). Noble metals were still well distributed in the cross-sections of the TA-, TA + SW-, and SW + TA-treated catalysts.

Average noble metal particle sizes (diameters) of the TA-, SW + TA-, and TA + SW-treated catalysts were 50, 60, and 60 nm, respectively. Particle size distribution is presented in Fig. 2. It is important to notice that according to TEM studies, particles with the size <20 nm also existed in the catalyst samples. However, only the particles >20 nm were taken into account in the particle size analyses from the FESEM images because it was the minimum reliable detection limit. Particles were measured from the cross-sectional FESEM images with the aid of ImageJ-software (>500
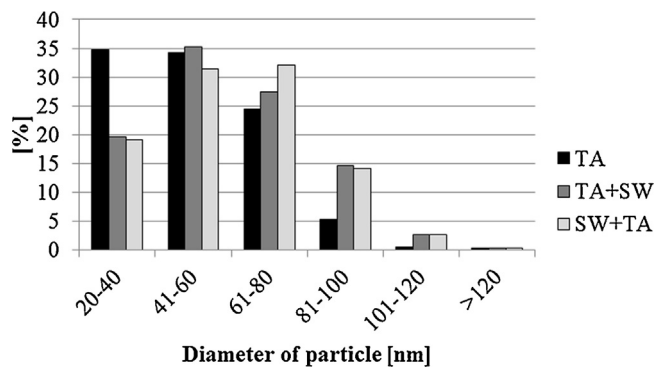
Fig. 2. Size distribution of the noble metal particles in the TA-, TA + SW, and SW + TA-treated catalysts (only particles with the diameter >20 nm were taken into account).

particles with size >20 nm were measured). Thus, in the results there is a bias towards the bigger particle sizes. However, the
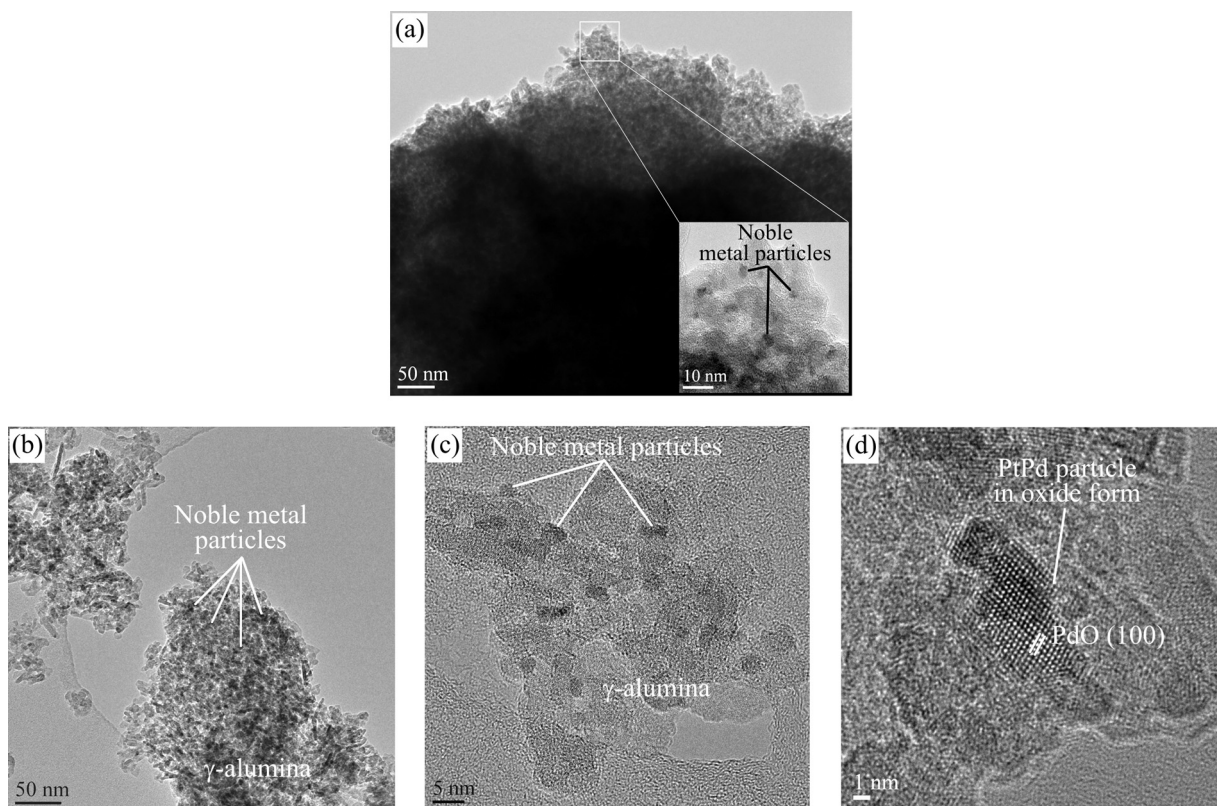
Fig. 3. TEM images of the fresh catalyst, (a) the cross-sectional sample, the inset with higher magnification and (b)–(d) the powdered sample with different magnifications.
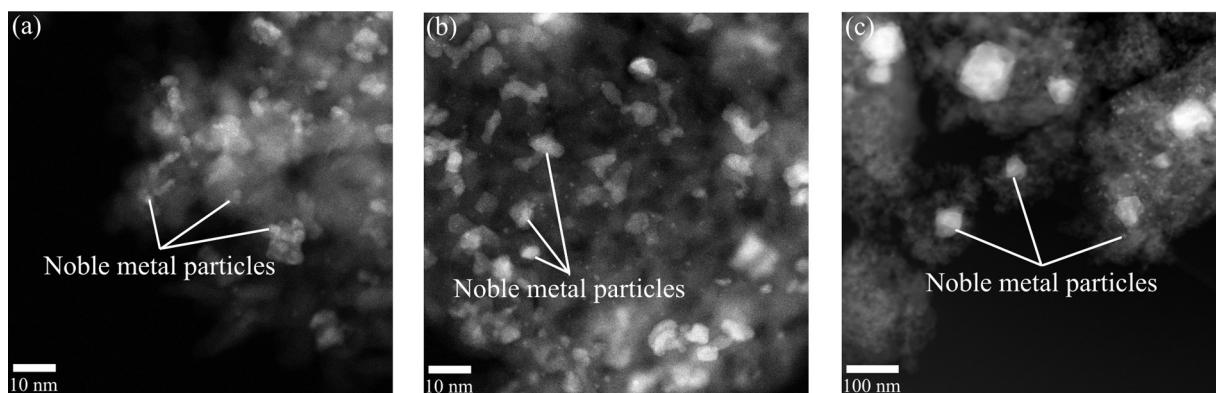
Fig. 4. STEM ADF images of the (a) fresh catalyst, (b) SW-treated catalyst, and (c) TA + SW-treated catalyst. Notice the different scale bar in (a) and (b) versus (c).
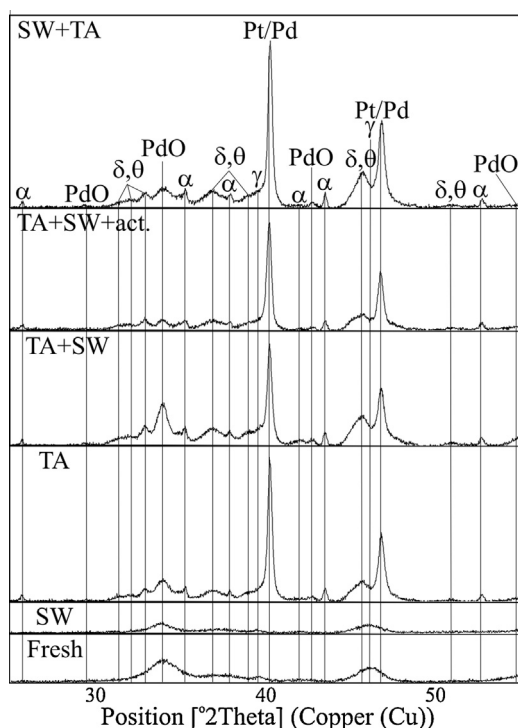

Fig. 5. XRD patterns of the fresh, sulfur-poisoned (SW), thermal-aged (TA), thermal-aged + sulfur-poisoned (TA+SW), thermal-aged + sulfur-poisoned after activity measurement (TA + SW + act.), and sulfur-poisoned + thermal-aged (SW + TA) catalysts ($\gamma = \gamma$-alumina, $\delta = \delta$-alumina, $\theta = \theta$-alumina, and $\alpha = \alpha$-alumina).

Table 3
Specific surface area, average pore size, and total pore volume of the fresh, SW-, TA-, TA + SW-, and SW + TA-treated catalysts.

	Fresh	SW	TA	TA + SW	SW + TA
Specific surface area [m^2/g]	154	147	96	96	92
Average pore size [nm]	10	10	14	14	15
Total pore volume [cm^3/g]	0.4	0.4	0.3	0.3	0.4

can be observed due to the relatively low concentration of noble metals.

In the SW-treated catalyst, the size of the noble metal particles seemed to be slightly increased (Figs. 4 (b) and 7) compared to the fresh catalyst. A slight increase in the crystallite size of PdO was observed also by XRD (Table 2); the amount of platinum was too small to be detected with XRD. According to our tentative study, no changes in the PtPd particles of the PtPd/γ-Al_2O_3 catalyst were observed after 400 °C for 5 h treatment in synthetic air (same temperature and exposure time than in the SW-treatment). Thus, a slight growth of the Pt/Pd particles seemed to be induced by presence of $SO_2 + H_2O$. According to the literature, sulfur and water vapor increase the mobility of the noble metal atoms, e.g., [18,23,24]. Based on the HRTEM studies, mainly PdO and PtO existed in the noble metal particles which agrees with XPS results (Fig. 6); despite the change in the binding energy of O 1s line, it can still be attributed to alumina [30]. TEM-EDS point analyses indicated both Pd and Pt in the noble metal particles as in the fresh catalyst. The specific surface area of the SW-treated catalyst was slightly decreased compared to the fresh catalyst (Table 3). This may be caused due to slight growth of the noble metal crystallites and sulfur species blocking some pore openings in the catalyst.

Significant morphological changes, due to the TA-treatments, were detected in them compared to the fresh and SW-treated catalysts. According to the TEM studies, morphology of the TA-, TA + SW-, and SW + TA-treated catalysts was similar. Based on the XRD results, in all thermally-treated catalysts γ-alumina changed to δ- and/or θ-alumina and to α-alumina (Fig. 5). Due to the phase transformation of alumina, the particle size of δ/θ-alumina and especially α-alumina increased compared to γ-alumina in the fresh catalyst. In addition, the size of the noble metal particles grew significantly under the thermal aging treatment (Figs. 4 (c) and 8) as already observed with FESEM indicating noble metal particles with a diameter of 50–60 nm. According to the HRTEM images (Fig. 8(c)), the grown noble metal particles consisted of several crystals. The particle had a bimetallic PtPd-alloy core surrounded by several PdO crystals. Based on the TEM-EDS results, cores consist of both Pt and Pd and the shells are Pd-rich. After the TA-, TA + SW- and SW + TA-treatments, both PdO and bimetallic Pt/Pd alloy were detected by XRD (Fig. 5). In the TA-, TA + TSW-, and SW+ TA-treated catalysts,

results can be used in the comparison of the large, agglomerated particles in all TA-treated catalysts. Based on the results, sizes of the formed large particles were similar after TA-, TA + SW-, and SW + TA-treatments.

Detailed structural characterization of the fresh and SW-, TA-, TA + SW-, and SW + TA-treated catalysts was carried out by TEMs, XRD, and XPS. In the fresh catalyst, noble metal particles, typically with a diameter of <5 nm, were well distributed in the small-grained γ-alumina surface (Figs. 3, 4 (a), Fig. 5 and Table 2). According to the TEM-EDS point analyses, the noble metal particles consisted of both Pt and Pd, however, the particles were Pd-rich. Pt:Pd loading in the catalyst was 1:4 wt-%. HRTEM images (Fig. 3) and XRD patterns (Fig. 5) indicated that Pd exists as PdO. The amount of platinum was too small to be detected with XRD. According to the binding energies of Pd (336.5 eV) and Pt (315.4 eV) in the XPS spectra (Fig. 6(a) and (b)), both exist in the oxide form [28,29]. In the O 1s spectrum (Fig. 6(c)), only oxygen originating from Al_2O_3

Table 2
Crystallite sizes of PdO and PtPd in the fresh, SW-, TA-, TA + SW-, and SW + TA-treated catalysts determined from the XRD spectra.

Size [nm]	Fresh	SW	TA	TA + SW	SW + TA
PdO[a] lattice parameters: $a = b = 3.0$ Å, $c = 5.3$ Å	3	6	9	9	8
PtPd[b] lattice parameters: $a = b = c = 3.9$ Å	–	–	26	31	27

[a] Determined from PdO-peak at $2\theta = 33.9°$ with the Scherrer equation (shape factor 0.9).
[b] Determined from Pd/Pt-peak at $2\theta = 40.1°$ with the Scherrer equation (shape factor 0.9).
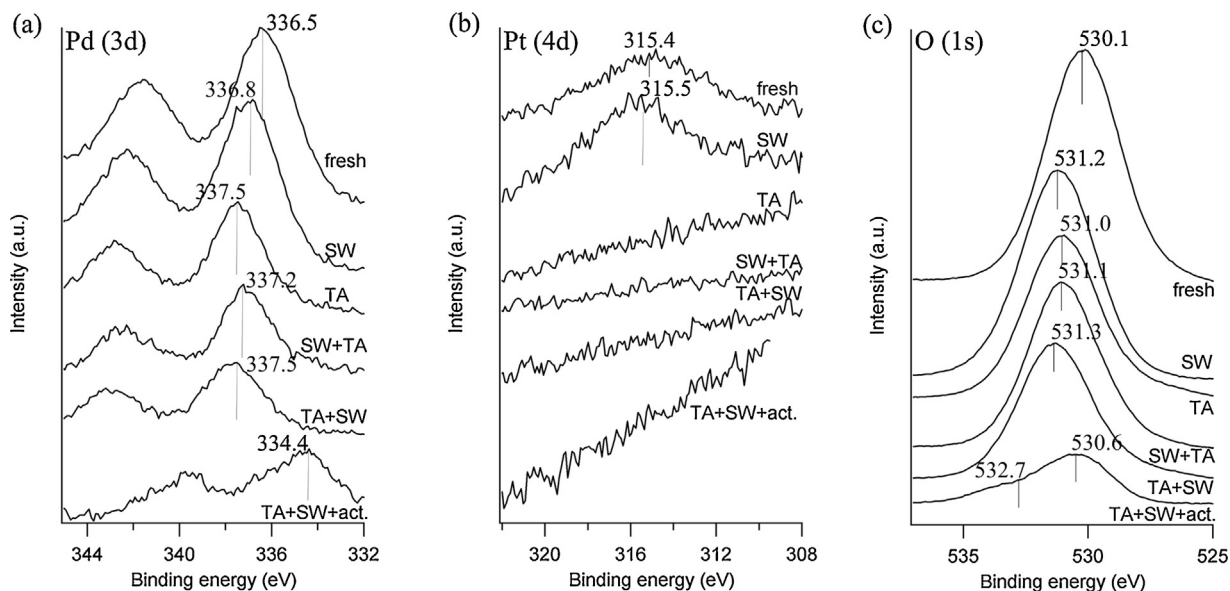
Fig. 6. XPS spectra and binding energies, (a) Pd 3d, (b) Pt 4d, and (c) O 1s spectra for the fresh, SW-, TA-, TA + SW, SW-TA- treated catalysts and TA + SW-treated catalyst after activity measurements.
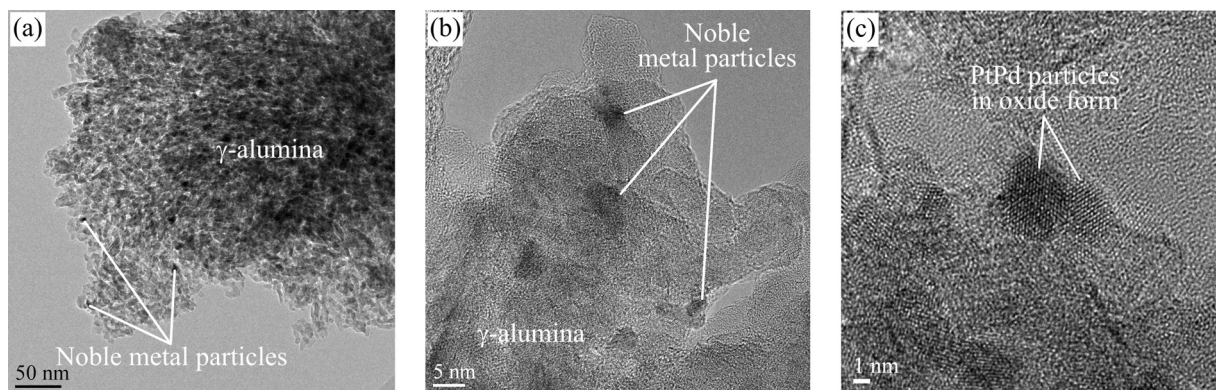
Fig. 7. TEM images of the SW-treated catalyst (the powdered sample), (a), (b), and (c) different magnifications.

the crystallite size of PdO was ~10 nm and that of PtPd was ~30 nm (Table 2) which agrees very well with TEM results. Pd was observed as an oxide [28], but metallic Pt and Pd are invisible in the XPS spectra (Fig. 6(a) and (b)) due to the PdO shell and the surface sensitivity of the technique. Similar grown noble metal particles were detected also in our earlier study concerning the lean-burn natural-gas-heavy-duty-vehicle-aged catalyst (160,000 km) [26]. Persson et al. reported that in thermal decomposition of PdO, Pd is incorporated into the Pt/Pd alloy in the Pd-Pt/Al$_2$O$_3$ catalyst [7]. Carrillo et al. reported that in the thermal aging in air at even 650 °C, small Pt particles formed mobile species which migrated and were trapped by PdO particles resulting in formation of PtPd particles [31]. Generally, decomposition of PtO to Pt happens above 350 °C and PdO to Pd at ~800 °C [3,32]. Johns et al. reported that after thermal aging in air at 750 °C for 10 h, Pt was fully reduced but almost 30% of the Pd

species were still in the oxide form [33]. In the thermally aged catalysts, in addition to the grown noble metal particles there were still also few, small noble metal particles with a diameter of ~5 nm (Figs. 4 (c) and 8 (d)). According to the TEM-EDS analyses, they contain both Pd and Pt and based on HRTEM images (Fig. 8(d)), they seemed to be single crystals in the metallic form indicating likely bimetallic PtPd particles. Small, likely bimetallic PtPd particles were hard to detect by XPS (Fig. 6(a) and (b)) because only few these kind of particles were observed by TEM. According to the literature [22], the position of the noble metal particles affects their sintering so that a valley position is much more stable than an on-top position. As a result, some particles at the valley position do not grow even at elevated temperature. Therefore, few small particles still existed after thermal treatment at 1000 °C; however, particles seemed to be reduced and formed bimetallic PtPd crystallites. The specific sur-
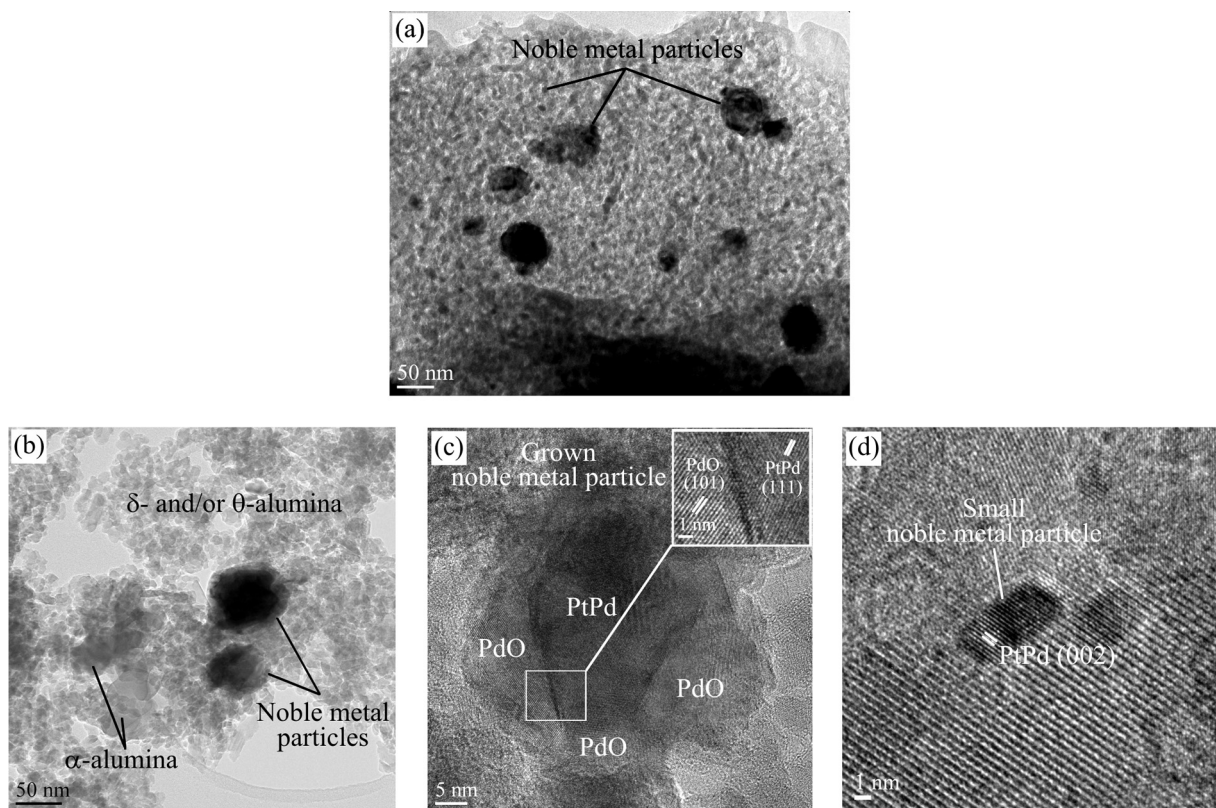
Fig. 8. TEM images of the TA + SW-treated catalyst, (a) the cross-sectional sample, (b), (c), and (d) the powdered sample with different magnifications.

face area decreased significantly (∼40%) and the average pore size increased (∼40%) during the TA-, TA + SW, and SW+TA-treatments compared to the fresh catalyst (Table 3) due to the significant growing of the noble metal particles and phase transformations of the washcoat followed by the crystal growth. SW-treatment after TA-treatment has no further effect on the specific surface area. It can be concluded that in the thermal treatment used in this study, the oxidized Pt totally reduces and partial decomposition of the oxidized Pd occurs followed by formation of the grown particles with a bimetallic PtPd core and a polycrystalline PdO shell. In addition there are still also few, small bimetallic PtPd particles.

3.2. Sulfur species on the catalyst

According to the FESEM-EDS and TEM-EDS analyses, in the SW- and TA + SW-treated catalysts sulfur existed uniformly through the whole catalyst structure from the inlet part to the outlet part and from the surface to the metallic monolith; the amount of sulfur was ∼3 wt-% which agrees well with XPS measurements. In the SW+TA-treated catalyst, no sulfur was detected. According to the literature, the sulfation process is reversible and SO_x from the catalyst surface easily desorbs and decomposes at elevated temperatures [15]. Based on the XPS S 2p spectrum (Fig. 9), sulfur is as sulfates [30]. In the O 1s spectra, the contribution of SO_4 species cannot be seen due to the domination of alumina and the possible overlapping of the binding energies of these two [30]. The DRIFT spectra of the SW- and TA + SW-treated catalysts (Fig. 10) have a broad band at around 1200–1100 cm^{-1} indicating bulk aluminum sulfate species [34,35]. The band around 1435 cm^{-1} attributed to $\nu S{=}O$ of stable Pd— or Pt—SO_4 species [34,36] is missing. Furthermore, any Pd $3d_{5/2}$ lines above 338 eV, which could be attributed to $PdSO_4$ [14], were not detected either by XPS. Bands around 1390–1300 cm^{-1} attributed to surface sulfate species on Al_2O_3 [16,34] or surface $Al_2(SO_3)_3$ [34] were not observed in the DRIFT spectra. According to Mowery and
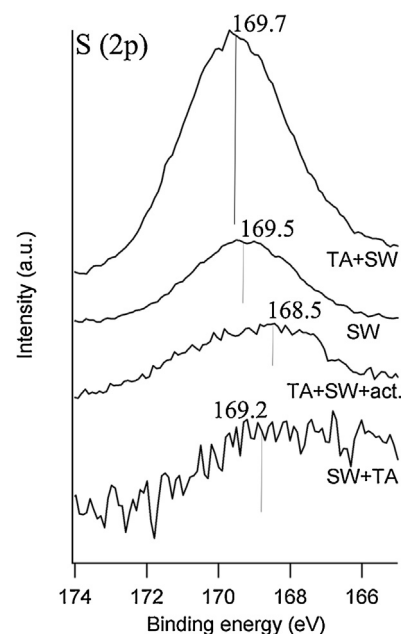

Fig. 9. XPS S 2p spectra for the SW-, TA-, TA + SW, SW-TA- treated catalysts and TA+SW-treated catalyst after activity measurements.

McCormick [14], sulfation of the PdO/Al_2O_3 catalyst happens by oxidation of SO_2 to SO_3 on PdO and SO_3 can form $PdSO_4$ on PdO or can migrate to Al_2O_3 forming $Al_2(SO_4)_3$. The strong band around 1030–1040 cm^{-1} is due to the catalyst material as it is present in all spectra including the fresh catalyst. It can be concluded that in the sulfur treatment used in this study only a small amount of bulk aluminum sulfate formed but no sulfur compounds on noble metals can be detected.
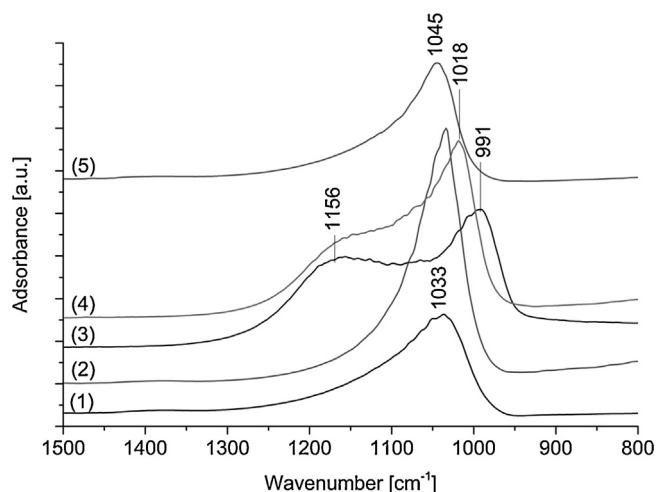
Fig. 10. DRIFT spectra for the (1) fresh, (2) TA-, (3) SW-, (4) TA + SW-, and (5) SW + TA-treated catalysts.

Fig. 12. CH_4 conversions as a function of temperature for the fresh, SW-, TA-, SW + TA-, and TA+SW-treated catalysts. For the TA + SW-treated catalyst two runs are presented.

Table 4
Light-off temperatures (T_{50} and T_{90}) for the fresh, SW-, TA-, SW + TA-, and TA + SW-treated catalysts. For TA + SW-treated catalyst values are presented after the first and the second run.

Catalyst	T_{50} [°C]	T_{90} [°C]
Fresh	390	488
SW	437	550
TA	445	570
SW + TA	441	552
TA + SW (first run)	564	–
TA + SW (second run)	498	–

According to the EELS maps, in the SW-treated catalyst sulfur existed mainly close to the noble metal particles (Fig. 11(a)) while in the TA + SW-treated catalyst it existed randomly distributed in the catalyst (Fig. 11(b)). Probably, small noble metal particles are very active to adsorb and oxidize sulfur species and $Al_2(SO_4)_3$ forms near the noble metal particles. While, the grown noble metal particles may be not so active to adsorb and oxidize sulfur species resulting in that $Al_2(SO_4)_3$ forms randomly over the noble metal particles and support. According to Smirnov et al. [37], at temperatures above 300 °C sulfate species form on the Al_2O_3 thin film without noble metal particles. Thus, it can be assumed that $Al_2(SO_4)_3$ can form also straight with the alumina support. In addition, due to the thermal aging treatments γ-alumina changed to δ-,θ-, and α-alumina which may affect the sulfation phenomenon of the support in the TA + SW-treated catalyst.

3.3. Activity of the catalyst

Conversions of CH_4 as a function of temperature over the fresh catalyst and SW-, TA-, TA + SW- and SW + TA-treated catalysts are presented 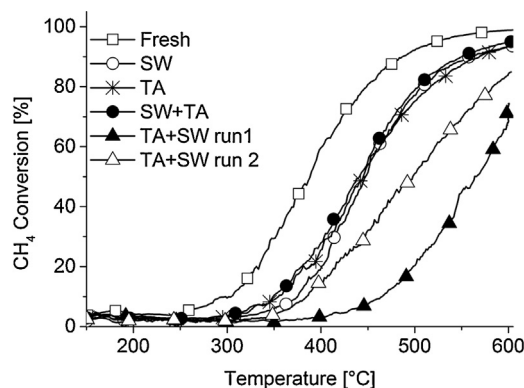in Fig. 12 and the light-off temperatures (T_{50} and T_{90}) are collected into Table 4. In general, laboratory-scale thermal treatment and/or sulfur exposure decreased the activity of the catalyst. Methane oxidation over the treated samples started at least 100 °C higher temperatures compared to the fresh catalyst and the light-off temperatures (T_{50}) were observed to increase at least by 50 °C compared to the fresh catalyst. The activities of the TA-, SW-, and SW + TA-treated catalysts were similar and the activity of the TA + SW-treated catalyst was notably lower than that of the other catalysts. The reason why in all the TA-treated catalyst the activity is decreased is due to the significant morphological changes compared to the fresh catalyst. Due to the growing of the noble metal particles, the amount of active sites decreased. In addition, phase
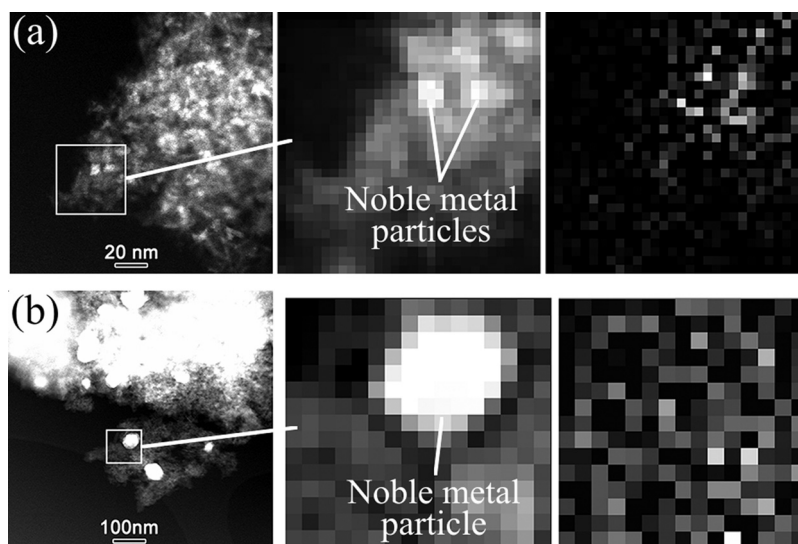

Fig. 11. The STEM ADF image, the enlarged STEM ADF image, and the STEM EELS sulfur map from the selected area (brighter color indicates higher amount) for (a) the SW-treated catalyst and (b) the TA + SW-treated catalyst. Notice the different scale bar in (a) and (b).

transformation of γ-alumina to δ/θ- and α-alumina significantly decreased specific surface area of the TA-treated catalyst (Table 3). According to the literature [17], phase transformation of γ-Al_2O_3 to θ-Al_2O_3 causes the reconstruction of the surface decreasing reactive sites of the support. In the SW-treated catalyst, slight increasing in the size of the noble metal particles and formation of $Al_2(SO_3)_4$ species close to the noble metal particles was detected which are probably blocking active sites followed by decreased conversion of methane. According to the literature [16], presence of SO_2 creates Brönsted acid sites on the γ-Al_2O_3 support while the fresh Pd/Al_2O_3 catalyst has only more reactive Lewis acid sites. Probably, this kind of changing in the acidity of the γ-Al_2O_3 support happens also in our SW-treatment causing further decreased activity of the SW-treated catalyst. In the TA + SW-treated catalyst, these above mentioned changes in the TA-treated and SW-treated catalysts are combined resulting in dramatic decreasing in the methane conversion. In the SW+TA-treated catalyst, formed $Al_2(SO_3)_4$ decomposed during TA-treatment resulting in similar catalyst activity to the TA-treated catalyst. Thus, formation of aluminum sulfate randomly over the TA + SW-treated catalyst has a significant effect on the catalyst deactivation.

The catalyst activity tests were done twice (run 1 and run 2); notable differences between run 1 and run 2 were observed only with the TA + SW-treated catalyst. Its activity was higher in the latter run indicating partial regeneration, i.e., decomposition of sulfate, of the catalyst. Thus, a short time (15 min) at 600 °C is enough to remove some sulfates from the catalyst. According to the FESEM-EDS analyses and XPS measurements, during the activity tests the amount of sulfur in the TA+SW-treated catalyst decreased from ∼3 wt-% to <1 wt-%. In addition based on the XPS results (Fig. 6(a)), PdO reduced during the activity tests of the TA+SW-treated catalyst. Also a shoulder, indicating another chemical state, was observed in its O 1s spectrum (Fig. 6(c)). A possible origin for this is by-products of methane combustion, such as hydroxides or carbon compounds. The reduction of PdO was also detected by XRD (Fig. 5). According to the literature, e.g., [38,39], PdO is reduced by CH_4. However, no significant reduction of PdO was observed by XRD in the SW- or SW + TA-treated catalysts during the activity tests. In the future, more characterization will be needed for activity-tested samples to study comprehensively their structure in the working state.

4. Conclusions

Accelerated deactivation phenomena in the PtPd/γ-Al_2O_3 natural-gas oxidation catalyst caused by thermal aging and/or sulfur + water poisoning were studied. Thermal aging and sulfur + water poisoning treatments were performed separately and with varied combinations. Comprehensive characterization of the catalyst was carried out after each step to get knowledge about existing of sulfur and influence of thermal aging before or after sulfur poisoning. The fresh catalyst contains oxidized Pt and Pd particles (<5 nm) uniformly distributed in the γ-alumina surface. In the SW-treated catalyst, a slight growing of the noble metal particles was observed. In addition, a small amount of bulk aluminum sulfate was detected near the noble metal particles. In the thermal aging, γ-alumina changed to δ- and/or θ- and α-alumina. In addition, total decomposition of oxidized Pt and partly decomposition of oxidized Pd occurred resulting in the formation of grown noble metal particles (50–60 nm) with a bimetallic PtPd core (∼30 nm) and a polycrystalline PdO (∼10 nm) shell. In addition, few, small (∼5 nm) and likely bimetallic PtPd particles were present in the catalyst as well. The noble metal particles and washcoat remained similar regardless of sulfur + water treatment before or after thermal aging. In the TA+SW-treated catalyst, a small amount of bulk alu-

minum sulfate was observed randomly distributed over the noble metal particles and support. In general, laboratory-scale thermal aging and/or sulfur poisoning decreased the activity of the catalyst. CH_4 conversion curves of the SW-, TA-, and SW + TA-treated catalysts were similar; their light-off temperatures T_{50} were higher compared to the fresh catalyst. The activity of the TA + SW-treated catalyst was the lowest, however, the activity recovered partly after the first activity run (heating up to 600 °C) indicating partial regeneration. Thus, combined morphological changes and sulfate on the catalyst decreased significantly the activity of the catalyst.

References

[1] P. Gélin, M. Primet, Appl. Catal. B Environ. 39 (2002) 1–37.
[2] E.M. Holmgreen, M.M. Yung, U.S. Ozkan, Appl. Catal. B Environ. 74 (2007) 73–82.
[3] R.J. Farrauto, J.K. Lampert, M.C. Hobson, E.M. Waterman, Appl. Catal. B Environ. 6 (1995) 263–270.
[4] A.K. Datye, J. Bravo, T.R. Nelson, P. Atanasova, M. Lyubovsky, L. Pfefferle, Appl. Catal. A Gen. 198 (2000) 179–196.
[5] M. Lyubovsky, L. Pfefferle, Catal. Today 47 (1999) 29–44.
[6] Y. Ozawa, Y. Tochihara, A. Watanabe, M. Nagai, S. Omi, Appl. Catal. A Gen. 259 (2004) 1–7.
[7] K. Persson, L.D. Pfefferle, W. Schwartz, A. Ersson, S.G. Järås, Appl. Catal. B Environ. 74 (2007) 242–250.
[8] K. Persson, K. Jansson, S. Jarås, J. Catal. 245 (2007) 401–414.
[9] N.M. Kinnunen, J.T. Hirvi, M. Suvanto, T.A. Pakkanen, J. Mol. Catal. A Chem. 356 (2012) 20–28.
[10] A.K. Neyestanaki, F. Klingstedt, T. Salmi, D.Y. Murzin, Fuel 83 (2004) 395–408.
[11] J.K. Lampert, M. Shahjahan, R.J. Farrauto, Appl. Catal. B Environ. 14 (1997) 211–223.
[12] A.T. Gremminger, H.W. Pereira de Carvalho, R. Popescu, J.-D. Grunwaldt, O. Deutschmann, Catal. Today (2015) 1–11.
[13] G. Corro, C. Cano, J.L.G. Fierro, J. Mol. Catal. A Chem. 315 (2010) 35–42.
[14] D.L. Mowery, R.L. McCormick, Appl. Catal. B Environ. 34 (2001) 287–297.
[15] O. Kröcher, M. Widmer, M. Elsener, D. Rothe, Ind. Eng. Chem. Res. 48 (2009) 9847–9857.
[16] M. Konsolakis, I.V. Yentekakis, G. Pekridis, N. Kaklidis, a. C. Psarras, G.E. Marnellos, Appl. Catal. B Environ. 138-139 (2013) 191–198.
[17] R. Wischert, C. Copéret, F. Delbecq, P. Sautet, Angew. Chemie. Int. Ed. 50 (2011) 3202–3205.
[18] C.H. Bartholomew, Appl. Catal. A Gen. 212 (2001) 17–60.
[19] T.W. Hansen, A.T. Delariva, S.R. Challa, A.K. Datye, Acc. Chem. Res. 46 (2013) 1720–1730.
[20] P.J.F. Harris, Int. Mater. Rev. 40 (1995) 97–115.
[21] J.A. Moulijn, A.E. Van Diepen, F. Kapteijn, Appl. Catal. A Gen. 212 (2001) 3–16.
[22] G.S. Parkinson, Z. Novotny, G. Argentero, M. Schmid, J. Pavelec, R. Kosak, P. Blaha, U. Diebold, Nat. Mater. 12 (2013) 724–728.
[23] A. Martínez, M.A. Arribas, M. Derewinski, A. Burkat-Dulak, Appl. Catal. A Gen. 379 (2010) 188–197.
[24] A.M. Azad, M.J. Duran, A.K. McCoy, M.A. Abraham, Appl. Catal. A Gen. 332 (2007) 225–236.
[25] H. Arai, M. Machida, Appl. Catal. A Gen. 138 (1996) 161–176.
[26] M. Honkanen, M. Kärkkäinen, V. Viitanen, H. Jiang, K. Kallinen, M. Huuhtanen, M. Vippola, J. Lahtinen, R. Keiski, T. Lepistö, Top. Catal. 56 (2013) 576–585.
[27] M. Aronniemi, J. Sainio, J. Lahtinen, Surf. Sci. 578 (2005) 108–123.
[28] M. Brun, A. Berthet, J.C. Bertolini, J. Electron. Spectrosc. Relat. Phenom. 104 (1999) 55–60.
[29] J.Z. Shyu, K. Otto, Appl. Surf. Sci. 32 (1988) 246–252.
[30] J.F. Moulder, W.F. Stickle, P.E. Sobol, K.D. Bomben, Handbook of X-ray Photoelectron Spectroscopy, Physical Electronics, Inc., Eden Prairie, 1995.
[31] C. Carrillo, T.R. Johns, H. Xiong, A. DeLaRiva, S.R. Challa, R.S. Goeke, K. Artyushkova, W. Lei, C.H. Kim, A.K. Datye, J. Phys. Chem. Lett. 5 (2014) 2089–2093.
[32] K. Hauff, U. Tuttlies, G. Eigenberger, U. Nieken, Appl. Catal. B Environ. 123–124 (2012) 107–116.
[33] T.R. Johns, J.R. Gaudet, E.J. Peterson, J.T. Miller, E.A. Stach, C.H. Kim, M.P. Balogh, A.K. Datye, ChemCatChem 5 (2013) 2636–2645.

[34] H. Abdulhamid, E. Fridell, J. Dawody, M. Skoglundh, J. Catal. 241 (2006) 200–210.
[35] H. Mahzoul, L. Limousy, J.F. Brilhac, P. Gilot, J. Anal. Appl. Pyrolysis 56 (2000) 179–193.
[36] S. Colussi, A. Trovarelli, E. Vesselli, A. Baraldi, G. Comelli, G. Groppi, J. Llorca, Appl. Catal. A Gen. 390 (2010) 1–10.
[37] M.Y. Smirnov, A.V. Kalinkin, A.V. Pashis, A.M. Sorokin, A.S. Noskov, K.C. Kharas, V.I. Bukhtiyarov, J. Phys. Chem. B 109 (2005) 11712–11719.
[38] P. Castellazzi, G. Groppi, P. Forzatti, Appl. Catal. B Environ. 95 (2010) 303–311.
[39] Z. Li, G.B. Hoflund, J. Nat. Gas Chem. 12 (2003) 153–160.